The Astrophysical Journal, 866:18 (15pp), 2018 October 10 https://doi.org/10.3847/1538-4357/aad806

Three-dimensional MHD Simulation of Solar Wind Using a New Boundary Treatment: Comparison with In Situ Data at Earth

Fang Shen[1,2,3], Zicai Yang[1,2], Jie Zhang[4], Wenwen Wei[1,2], and Xueshang Feng[1,2,3]
[1] SIGMA Weather Group, State Key Laboratory of Space Weather, National Space Science Center, Chinese Academy of Sciences, Beijing 100190, People's Republic of China; fshen@spaceweather.ac.cn
[2] University of Chinese Academy of Sciences, Beijing 100049, People's Republic of China
[3] HIT Institute of Space Science and Applied Technology, Shenzhen 518055, People's Republic of China
[4] Department of Physics and Astronomy, George Mason University, Fairfax, VA 22030, USA
Received 2018 July 12; revised 2018 July 28; accepted 2018 July 30; published 2018 October 5

Abstract

Three-dimensional magnetohydrodynamics (MHD) numerical simulation is an important tool in the prediction of solar wind parameters. In this study, we improve our corona interplanetary total variation diminishing MHD model by using a new boundary applicable to all phases of solar cycles. This model uses synoptic magnetogram maps from the Global Oscillation Network Group as the input data. The empirical Wang–Sheeley–Arge relation is used to assign solar wind speed at the lower boundary, while temperature is specified accordingly based on its empirical relation with the solar wind speed. Magnetic field intensity and solar wind density at the boundary are obtained from observational data in the immediate past Carrington rotations, permitting the persistence of these two parameters in a short time period. The boundary conditions depend on only five tunable parameters when simulating the solar wind for different phases of the solar cycle. We apply this model to simulate the background solar wind from 2007 to 2017 and compare the modeled results with the observational data in the OMNI database. Visual inspection shows that our model can capture the time patterns of solar wind parameters well at most times. Statistical analysis shows that the simulated solar wind parameters are all in good agreement with the observations. This study demonstrates that the improved interplanetary total variation diminishing model can be used for predicting all solar wind parameters near the Earth.

Key words: magnetohydrodynamics (MHD) – methods: numerical – solar wind – Sun: heliosphere

Supporting material: extended figure

1. Introduction

The prediction of solar wind plasma and magnetic field parameters near the Earth is scientifically challenging and carries significant application values (Feynman & Gabriel 2000). Numerical technology plays an important role in the prediction of solar wind parameters. Over the years, a variety of techniques have been developed to predict the state of the solar wind that vary from purely statistical approaches to physics-based models (Riley et al. 2017 and references therein). In particular, magnetohydrodynamics (MHD) numerical models, including hybrid empirical/physics-based models and full physics-based models, are important tools in this endeavor (e.g., Owens et al. 2008; Gressl et al. 2014; Jian et al. 2015). The distribution and propagation of the solar wind from the Sun to the Earth, as well as the solar wind conditions near the Earth, have been determined to a good extent through MHD simulation.

Existing MHD models vary significantly in how they treat the corona domain and the condition at the boundary (hereafter the lower boundary) that connects the inner corona domain and the outer heliospheric domain. In full physics-based coupled-corona-heliosphere three-dimensional (3D) MHD models, including the CSEM model developed by Tóth et al. (2012) and the SIP-CESE MHD model by Feng et al. (2007), coronal heating processes and radiation transfer effects are explicitly addressed in the MHD equations, thus deriving properties of the background solar wind from the first principle. In the hybrid empirical/physics-based 3D models, e.g., the Wang–Sheeley–Arge (WSA)-ENLIL model by Odstrcil (2003), the physical process in the corona is neglected, since the lower boundary is usually located at ~0.1 au, which is beyond the coronal region. Instead, the lower-boundary conditions of the WSA-ENLIL model are provided by an empirical coronal solution (e.g., Odstrcil 2003 and references therein). Full 3D MHD models are computationally demanding, especially in the coronal region, because the plasma β near the solar surface is low ($\beta \ll 1$), which results in a very small time-step size determined by the Courant–Friedrichs–Levy condition during simulation. On the other hand, the hybrid empirical/physics-based 3D models use the empirical relation at the lower boundary, thus saving many computing resources in the 3D coronal region. In recent years, many comparative studies have been carried out to evaluate the prediction capability of these models by comparing with actual observations at Earth (e.g., Owens et al. 2008; Lee et al. 2009; Gressl et al. 2014; Jian et al. 2015). They found that, at this stage of development, the hybrid models are comparable with the full physics-based model in reproducing the large-scale structure of the solar wind. Therefore, with respect to time efficiency and prediction accuracy, the hybrid empirical/physics-based models remain an important tool in the prediction of solar wind parameters in the near future.

The treatment of the lower-boundary condition plays a crucial role in the hybrid empirical/physics-based models, especially in influencing the consistency between the simulation results and the observations over the long term, e.g., over

solar cycles. Previous studies (e.g., Owens et al. 2008) revealed that further tuning of the lower boundary of heliospheric models could significantly improve the model performance. There are different kinds of lower-boundary conditions in the existing hybrid models (e.g., Odstrcil 2003; Detman et al. 2006, 2011; Hayashi 2012; Wiengarten et al. 2014). In the WSA/ENLIL model (Odstrcil 2003), the lower boundary is determined from the WSA model, which uses photospheric magnetic maps as input to get the magnetic field and solar wind speed. In addition, an assumption of constant momentum flux is used to derive the mass density, and the temperature is chosen to ensure that the total pressure (sum of thermal and magnetic pressures) is uniform on the source surface. The Hybrid Heliospheric Modeling System developed by Detman et al. (2006) is composed of both physics-based models and empirical models. In these models, the lower boundary is set at 0.1 au (21.5 R_s), where the radial magnetic field is given by combining a potential field source surface (PFSS) model with the Schatten current-sheet model (Schatten 1971). An empirical relationship between the magnetic flux tube expansion factor and solar wind speed at 0.1 au is a key element of the system. Then the value of V_r from the assumption of constant mass flux is used to specify the value of the mass density. Finally, the temperature is based on the assumption that the total of the magnetic and thermal pressures is a constant. Based on the work by Detman et al. (2006, 2011), Hayashi (2012) presented a treatment of observation-based time-dependent boundary conditions for the lower boundary at 50 R_s, where the radial magnetic fields are obtained by using a PFSS model and the WSO solar photospheric magnetic field data, the solar wind speed is specified by the interplanetary scintillation solar wind data, and the density and temperature are obtained by the *Helios* observations. Wiengarten et al. (2014) used 10 R_s as the lower boundary in their MHD simulation, the input data of magnetic fields are the result of solar surface flux transport modeling using observational data of sunspot groups coupled with a current-sheet source surface model, and other parameters are obtained following an empirical relation by using an inverse relation between flux tube expansion and radial solar wind speed (Detman et al. 2006, 2011).

However, these treatments of boundary conditions mentioned above are not self-consistent to a certain extent, which may contribute to the existing discrepancy between simulation results and observations in the interplanetary space. In this paper, based on our previous 3D corona interplanetary total variation diminishing (COIN-TVD) MHD model (Feng et al. 2003, 2005; Shen et al. 2007, 2009, 2011a, 2014), we change the lower boundary to 0.1 au and propose and implement a new method of treating the lower-boundary condition in a more self-consistent way. This is the base of establishing a high-performance hybrid empirical and 3D heliospheric MHD model, now called the improved 3D interplanetary TVD (IN-TVD) MHD model. In this model, we set several free parameters as a constant and only employ five time-varying free parameters, so as to simulate the solar wind for different phases of the solar cycle. In particular, our method can significantly improve the prediction of magnetic fields near the Earth, which has been problematic in most other models.

In Section 2, we give a detailed description of the improved 3D IN-TVD MHD model. In Section 3, we present a new set of boundary conditions based on the WSA model and constrained by observations of the solar wind in the past. In Section 4, we present the results of simulations from 2007 to 2017 using the improved 3D IN-TVD MHD model with the new boundary treatment. The comparison with the OMNI observations is also carried out in this section. In the last section, a discussion and summary are given.

2. The Numerical Model—The Improved IN-TVD Model

Our previous COIN-TVD model consists of a set of 3D MHD numerical models that combine calculations in two spatial domains (Feng et al. 2003, 2005). In this model, the 3D MHD equations are solved through a time-relaxation numerical technique in the corona and a marching-along-radius method in the heliosphere. Shen et al. (2007, 2009) made a modification to the 3D COIN-TVD model to realize the whole time-dependent simulation from the solar surface to 1 au by applying an asynchronous and parallel time-marching method during the simulation. Using this model, Shen et al. (2011a, 2011b, 2012a, 2012b, 2013, 2014) made a series of simulations to multiple real coronal mass ejection (CME) events and successfully showed the 3D scenes of CME propagation and CME–CME interaction in the corona and heliosphere. Their simulations can reproduce the general characteristics of CMEs shown in remote-sensing imaging observations of satellites and provide a relatively satisfactory comparison with solar wind plasma parameters obtained from in situ observations at 1 au. Nevertheless, there still exists significant quantitative disagreement. To improve the precision of the model prediction and at the same time conserve the model efficiency, we have made an improvement to the 3D COIN-TVD model, explained in the following equations:

$$\frac{\partial \rho}{\partial t} + \nabla \cdot (\rho \boldsymbol{V}) = 0, \tag{1}$$

$$\frac{\partial \rho \boldsymbol{V}}{\partial t} + \nabla \cdot \left[\left(P + \frac{B^2}{2\mu_0} \right) \boldsymbol{I} + \rho \boldsymbol{V}\boldsymbol{V} - \frac{\boldsymbol{B}\boldsymbol{B}}{\mu_0} \right] = -\frac{\rho G M_s}{r^2} \frac{\boldsymbol{r}}{r} + \boldsymbol{V} \cdot \boldsymbol{f}, \tag{2}$$

$$\frac{\partial \boldsymbol{B}}{\partial t} + \nabla \cdot (\boldsymbol{V}\boldsymbol{B} - \boldsymbol{B}\boldsymbol{V}) = 0, \tag{3}$$

$$\frac{\partial P}{\partial t} + \nabla \cdot (\rho \boldsymbol{V}) = -(\gamma - 1) P \nabla \cdot \boldsymbol{V}, \tag{4}$$

where μ_0 is the magnetic permeability in free space, G is the gravitational constant, M_s is the solar mass, and $\boldsymbol{I}$ denotes the unit tensor. Proton and electron temperatures are assumed to be equal and are determined from the ideal gas law $p = 2NkT$, where k is the Boltzmann constant and N is the number density of protons ($\rho = N(m_p + m_e)$, where m_p is the proton mass and m_e is the electron mass). The polytrophic index γ is an important parameter in MHD simulations. Using data from *Helios*, Totten et al. (1995) derived the empirical polytrophic index to be 1.46. Therefore, we employ this constant polytrophic index everywhere in the simulation domain.

It is convenient to perform calculations in a frame of reference corotating with the Sun. The coordinate frame is assumed to rotate around the solar rotation axis so that the boundary conditions at the inner surface remain fixed in the computation. Based on the coordinate transformation theory,

additional fictitious force densities, $\boldsymbol{f} = -\Omega \times [\Omega \times \boldsymbol{r} + 2\Omega \times \boldsymbol{V}]$, should be introduced into the momentum equation, where Ω is the sidereal angular velocity of the rotation. Although the Sun's photosphere rotates differentially, we neglect this longer timescale effect in predicting the solar wind at 1 au for the sake of convenience and thus choose a constant solar angular rotation speed $\Omega = 14.71\,\mathrm{deg\ day^{-1}}$, which corresponds to the sidereal rotation period of 24.47 days (Snodgrass & Ulrich 1990; Wiengarten et al. 2014). This $\boldsymbol{f}$ term is essential in the simulation, since it is exactly the main factor that leads to the stream–stream interaction and the redistribution of the profiles of the solar wind parameters in interplanetary space.

In the numerical scheme of the 3D model, all of the physical quantities are computed from the conservation TVD Lax–Friedrich scheme in a Sun-centered spherical coordinate system. In order to enforce the $\nabla \cdot \boldsymbol{B} = 0$ constraint, an artificial diffusivity is added at each time step, following the completion of the TVD Lax–Friedrich scheme (van der Holst & Keppens 2007; Rempel et al. 2009; Feng et al. 2010). In this way, the $\nabla \cdot \boldsymbol{B}$ error produced by the scheme is diffused away at the maximal rate allowed by iterating

$$\boldsymbol{B} := \boldsymbol{B} + \mu(\Delta x)^2 \nabla\nabla \cdot \boldsymbol{B}, \tag{5}$$

where $(\Delta x)^2 = \frac{1}{\frac{1}{(\Delta r)^2} + \frac{1}{(r\Delta\theta)^2} + \frac{1}{(r\sin\theta\Delta\phi)^2}}$. For values of $\mu \in (0, 2)$, typically less than 10 iterations are sufficient to satisfy $\max\left(\frac{\int\int B_n ds}{\int\int |B_n| ds}\right) \leqslant 10^{-2}$. This artificial diffusivity can lead to a scheme that is fully shock capturing, at least to second-order accuracy in smooth regions.

To model the solar wind in interplanetary space, the lower boundary is set to be located at the base of the supersonic flow region, which is usually between 18 and 30 R_s (e.g., Odstrcil 2003; Detman et al. 2006; McGregor et al. 2011; Shiota et al. 2014; Wiengarten et al. 2014). The highest radial Alfvén critical point around solar minimum may be located between 10 and 14 R_s, below which the effect of solar rotation can be neglected and stream–stream interactions are unimportant (Zhao & Hoeksema 2010). Therefore, the inner radial grid boundary can be chosen to be located at 21.5 R_s (0.1 au), well beyond the Alfvén critical surfaces. The solar wind speed is super-Alfvénic everywhere in the computational domain. Thus, perturbations cannot travel toward the Sun, and constant boundary conditions can be chosen in the corotating frame with the assumption that a steady solar wind structure can last for one Carrington rotation (CR). Beyond the lower boundary, stream–stream interactions become more and more important and cannot be neglected.

The computational domain covers $21.5\ R_s \leqslant r \leqslant 258\ R_s$ (0.1–1.25 au), $-90° \leqslant \theta \leqslant 90°$, and $0° \leqslant \phi \leqslant 360°$, where r is the radial distance from the solar center in units of solar radius R_s and θ and ϕ are latitude and longitude, respectively. The radial grid is not uniform, and the total number is 202. The grid size gradually increases from 0.37 R_s at the lower boundary to 2.37 R_s near 1.25 au. To avoid the singularity in the spherical coordinate system, a six-component mesh grid system is used on the spherical shell (Feng et al. 2010). This grid system consists of six identical component meshes to envelope a spherical surface with partial overlap on their boundaries. Each component grid is a low-latitude spherical mesh, which is defined in the spherical coordinates by $(\frac{\pi}{4} - \delta \leqslant \theta \leqslant \frac{3\pi}{4} + \delta) \bigcap (-\frac{\pi}{4} - \delta \leqslant \phi \leqslant \frac{\pi}{4} + \delta)$, where δ is proportionally dependent on the grid spacing entailed for the minimum overlapping area. The grid resolution is $\Delta\phi = \Delta\theta = 1°$, corresponding to a time resolution of 1.8 hr. We use the six-component mesh grid system to improve the performance of our MHD model, mainly because each component grid is just a regular low-latitude part of the latitude–longitude grid, and the singularity in the spherical coordinate system can easily be avoided (Feng et al. 2010).

3. New Treatment of the Boundary

As the location of the lower boundary is beyond the Alfvén critical surface, all of the characteristic waves propagate outward, which means that a given boundary condition will determine the evolution of the solar wind in interplanetary space. Therefore, all eight of the MHD parameters should definitely be given at the lower boundary. Due to the lack of sufficient observational constraints, the solar wind parameters imposed on the lower boundary are derived from one input of data: a synoptic map of photospheric magnetic fields. In this paper, we use the synoptic maps provided by the Global Oscillation Network Group (GONG) project (http://gong.nso.edu/), in which six ground-based solar observatories worldwide cooperate.

In our model, the radial magnetic field at the lower boundary is calculated based on the PFSS model (Altschuler & Newkirk 1969; Schatten et al. 1969) with the input of synoptic maps. In the PFSS model, we use the source surface height of 2.5 R_s (Hoeksema et al. 1983). Although the PFSS model could be used to predict the interplanetary magnetic field (IMF) polarity quite well (Arge et al. 2003), it has a strong latitudinal variability, and the field strength increases in magnitude away from the neutral line, which is in conflict with the *Ulysses* spacecraft observations that showed no significant gradient with respect to heliomagnetic latitude in the radial component of the interplanetary magnetic field (Smith & Balogh 1995). Since the existing MHD models systematically underestimated the magnetic flux in the heliosphere (Stevens et al. 2012; Gressl et al. 2014), we only keep the polarity of the magnetic field from the PFSS model and use the observational data at 1 au in the immediate past to limit the value of the magnetic field,

$$B_r = \mathrm{sign}\,(B^{\mathrm{PFSS}}) \times \frac{1}{\sqrt{2}}\mathrm{mean}(B^{1\ \mathrm{au}})\left(\frac{1\ \mathrm{au}}{R_b}\right)^2, \tag{6}$$

where $\mathrm{mean}(B^{1\ \mathrm{au}})$ is the average value of the observed magnetic field at 1 au from the OMNI database during the past three CRs. Because $\mathrm{mean}|B_\phi| \approx \mathrm{mean}|B_r|$ at 1 au, B_0 is defined as $\frac{1}{\sqrt{2}}\mathrm{mean}(B^{1\ \mathrm{au}})$, the mean radial magnetic field at 1 au. After obtaining B_0, we can get the distribution of the magnetic field at the lower boundary by considering the magnetic flux conservation and the polarity from the PFSS model. This empirical method is based on the reasonable assumption that the overall magnetic field in the heliosphere is persistent over a few solar cycles.

The distribution of the solar wind speed at the lower boundary is very important for determining the distribution of other parameters, e.g., the density and temperature. In this study, the empirical WSA relation is used to assign solar wind speed. The WSA model is initially based on the observation that the speed of the solar wind measured at 1 au negatively

correlates with the magnetic flux tube expansion factor (f_s) near the Sun (Wang & Sheeley 1990). Then, it has been successively refined by combining with another parameter θ_b, which denotes the minimum angular separation between an open field foot point and its nearest coronal hole boundary (Arge et al. 2003). More generally, the solar wind velocity at 5 R_s can be expressed as a function of two coronal magnetic field parameters,

$$V_r = V_s + \frac{V_f}{(1+f_s)^{a_1}}\left[1 - 0.8\exp\left(-\left(\frac{\theta_b}{a_2}\right)^{a_3}\right)\right]^{a_4}, \quad (7)$$

where V_s is the slowest speed, V_f is the fastest speed, and a_1–a_4 are four additional free parameters in the model. Both f_s and θ_b can be obtained from the PFSS model. It should be noted that, however, some of these free parameters are adjusted for magnetograms from different observatories (Riley et al. 2015). Here we set $V_f = 675\,\mathrm{km\,s^{-1}}$, $a_1 = 0.22$, $a_3 = 1.0$, and $a_4 = 1.0$ as constants over time and keep two free parameters, V_s and a_2, that adjust with the phases of the solar cycle. In addition, the number of multipole components included in the spherical harmonic expansion in PFSS models, $L_{\max}$, can influence the distribution of f_s and θ_b to a good extent. Usually, increasing $L_{\max}$ can make f_s bigger and θ_b smaller. The distributions of f_s and θ_b are too simplistic when $L_{\max} < 5$, but the deviations of f_s and θ_b become small when $L_{\max} > 15$; they are nearly constant for most locations when $L_{\max} \geqslant 22$ (Poduval & Zhao 2004). In this model, we keep $L_{\max}$ as the primary regulatory factor and leave V_s and a_2 as the secondary regulatory parameters. The solar wind velocity at 21.5 R_s is obtained by taking the velocity given in Equation (7) and subtracting $50\,\mathrm{km\,s^{-1}}$ to account for the acceleration in the heliosphere (McGregor et al. 2011).

It is well known that there is a strong negative correlation between density and flow velocity (Neugebauer & Snyder 1966), which implies that the density cannot be taken as an unconstrained free parameter in solar wind models. Previous studies show that different observational data may give different quantitative relations between the solar wind speed and density (e.g., Burlaga & Ogilvie 1970; Steinitz & Eyni 1980; Phillips et al. 1995). Recently, using the observational data from *Helios*, *Ulysses*, and *Wind*, Le Chat et al. (2012) found that the approximation for the solar wind energy flux, $F_e = \rho V_r\left(\frac{1}{2}V_r^2 + \frac{GM_s}{R_s}\right)$, was largely independent of the solar wind speed and latitude, and this quantity varied weakly over the solar cycle. Based on their analysis, by setting the solar wind energy flux as a constant, the number density can be calculated by

$$N = N_0\left(\frac{1\,\mathrm{au}}{R_b}\right)^2 V_0\left(\frac{1}{2}V_0^2 + \frac{GM_s}{R_s}\right)\left[V_r\left(\frac{1}{2}V_r^2 + \frac{GM_s}{R_s}\right)\right]^{-1}, \quad (8)$$

where $R_b = 0.1$ au, and N_0 and V_0 are the number density and velocity at 1 au. Set $V_0 = 750\,\mathrm{km\,s^{-1}}$, and N_0 can be deduced from the average solar wind energy flux during the past three CRs at 1 au based on the OMNI observations. Some MHD models used the relation of $\rho \propto V_r^{-q}$, where $q = 1$ or 2 (e.g., Steinitz & Eyni 1980; Phillips et al. 1995). Detman et al. (2011) suggested that neither is quite uniform and that a parameter of the form ρV^q with $1 < q < 2$ might be better.

Table 1
Ranges of Free Parameters at the Lower Boundary

Free Parameters	$L_{\max}$	V_s (km s^{-1})	a_2 (deg)	B_0 (nT)	N_0 (cm^{-3})
Minimum	6	250	2.0	2.6	1.3
Maximum	15	300	4.0	5.3	2.7

The temperature can be specified in the same way as density on account of the relationship of $T - V$. The $T - V$ relationship at 1 au was quantified by Burlaga & Ogilvie (1970), and both linear and quadratic relationships between T and V have been obtained in later studies (e.g., Lopez & Freeman 1986; Richardson & Cane 1995; Elliott et al. 2005; Verbanac et al. 2011; Le Chat et al. 2012). Here we choose to use the relation that the proton temperature is a quadratic function of the velocity at 1 au: $T_p \sim \frac{1}{2}V_r^2$, with T_p in K and V_r in km s^{-1}. Then we normalize T_p to 0.1 au by the power law $T_p \sim \frac{1}{r^{2(\gamma-1)}}$ as the Parker solution (Parker 1958) of the case $\gamma = 1.46$, and we get the relationship of T_p and V_r at the lower boundary:

$$T_p = \frac{1}{2}V_r^2\left(\frac{1\,\mathrm{au}}{R_b}\right)^{2(\gamma-1)}. \quad (9)$$

Suppose that the proton temperature is equal to the electron temperature $T = T_p = T_e$, and we can obtain the pressure on the lower boundary: $p = 2NKT$.

When observed in the rest frame and supposing that the solar wind plasma flow propagates through the boundary in the radial direction, the meridional components V_θ and azimuthal flow velocity V_ϕ at the lower boundary in the corotation frame are determined by the following formulae:

$$V_\theta = 0, \quad V_\phi = -\Omega R_b \sin\theta. \quad (10)$$

When observed in the corotation frame, the magnetic field line would be parallel to the solar wind plasma flow at the steady state. Consequently, the two magnetic field vector components, B_θ and B_ϕ, are determined by the following formulae:

$$B_\theta = 0, \quad B_\phi = -\frac{\Omega R_b \sin\theta}{V_r}B_r. \quad (11)$$

Until now, we have specified all the physical parameters at the lower boundary. In order to make accurate predictions of the solar wind parameters, we use only five free parameters, while the other parameters are set to constants, as shown in Table 1. From 2007 to 2017, the range of V_s is very small, from 250 to 300 km s^{-1}; a_2 changes from 2.0 to 4.0, and $L_{\max}$ is from 6 to 15. Here B_0 and N_0 are restricted free parameters, as they are determined by solar wind data in previous CRs. A detailed analysis of how to tune the free parameters $L_{\max}$, V_s, and a_2 as the phase changes will be given in Section 4.2.

It should be noted that, instead of supposing the total pressure or thermal pressure to be constant on the surface at the lower boundary as other models did, we obtain the temperature and density from the solar wind speed using the relations discussed above. We believe that our method should reconstruct the temperature and density at the boundary in a more realistic way. After the lower boundary is given, the initial condition of all the parameters can be given as follows:

$$V_\alpha(r, \theta, \phi) = V_\alpha(R_b, \theta, \phi) \quad \text{where} \quad \alpha = r, \theta, \phi, \quad (12)$$

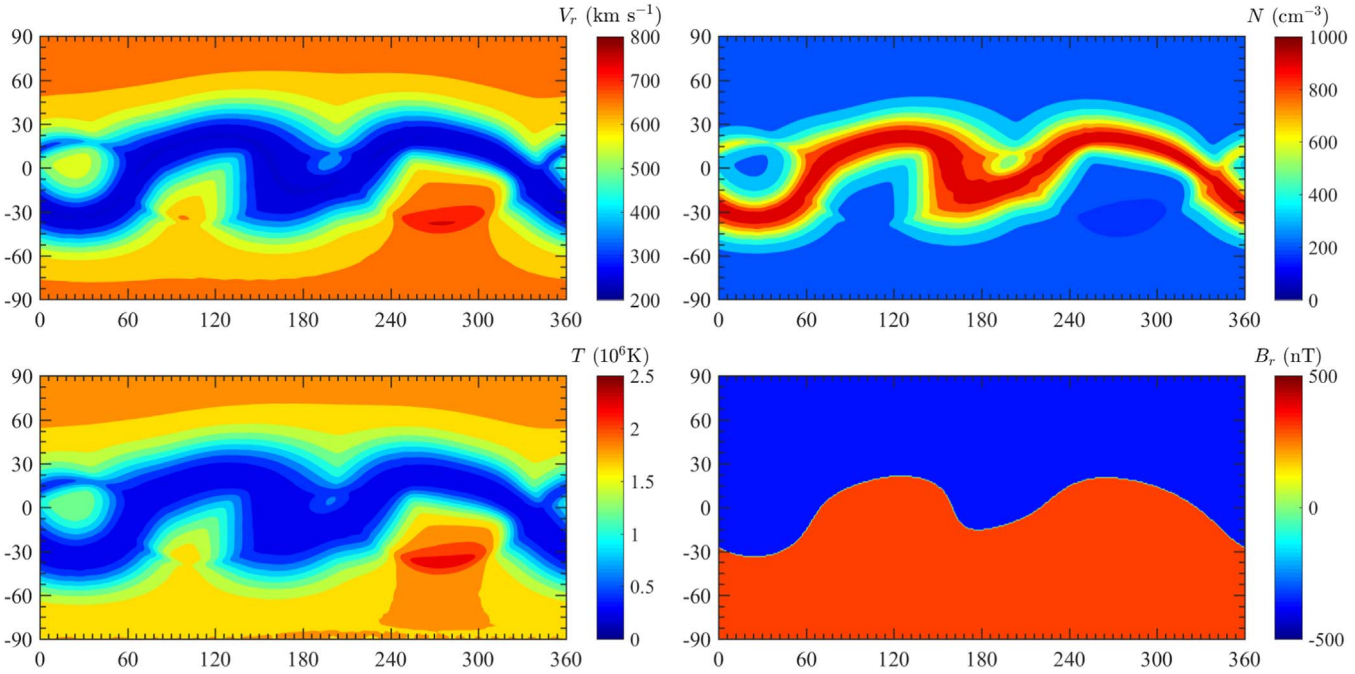

Figure 1. Maps of solar wind parameters at the lower boundary of 0.1 au for CR2053. From the upper left to the lower right, the panels show the radial velocity V_r (km s^{-1}), number density N (cm^{-3}), temperature T (K), and radial magnetic field B_r (nT). For each panel, the x axis is Carrington longitude, and the y axis is Carrington latitude in the Carrington coordinate system.

$$\rho(r, \theta, \phi) = \rho(R_b, \theta, \phi)\left(\frac{r}{R_b}\right)^{-2}, \quad (13)$$

$$T(r, \theta, \phi) = T(R_b, \theta, \phi)\left(\frac{r}{R_b}\right)^{-1}, \quad (14)$$

$$B_\alpha(r, \theta, \phi) = B_\alpha(R_b, \theta, \phi)\left(\frac{r}{R_b}\right)^{-2} \quad \text{where} \quad \alpha = r, \theta, \phi. \quad (15)$$

4. Simulation Results

In this section, we present the results of using the improved 3D IN-TVD model with the new lower-boundary conditions discussed above to simulate the background solar wind, covering the years from 2007 to 2017.

4.1. Results in 2007 (CR2051–CR2065)

First, we simulate the 3D distribution of the background solar wind in 2007, which was a time period of low solar activity during the late declining phase of solar cycle 23. For 2007, only two interplanetary coronal mass ejections (ICMEs) were identified in in situ plasma and field measurements at 1 au near the Earth (Richardson & Cane 2010), so this year is very suitable for the testing of solar wind models. The values of the free parameters that define the lower boundary for 2007 are listed in Table 2. Except for B_0 and N_0, which change with the CRs, the other three parameters are kept as a fixed value for the whole year: $L_{\max} = 6$, $V_s = 250\,\mathrm{km\,s^{-1}}$, and $a_2 = 2°$. We also notice that both B_0 and N_0 declined with time, and the maximum of the decrease is 18% and 14%, respectively.

As an example, by using CR2053 (from 2007 February 4 to March 4), Figure 1 shows color maps of the radial velocity V_r, number density N, temperature T, and radial magnetic field B_r at the lower boundary. At the boundary, the radial magnetic

Table 2
Values of the Free Parameters in Boundary Conditions from 2007 to 2017

CR	Start Time	V_s (km s^{-1})	a_2 (deg)	B_0 (nT)	N_0 (cm^{-3})	$L_{\max}$
2199	20171230	275	2.00	3.59	2.32	8
2198	20171203	275	2.00	3.55	2.31	8
2197	20171106	275	2.00	3.64	2.24	8
2196	20171010	275	2.00	3.76	2.11	8
2195	20170912	275	2.00	3.91	2.02	8
2194	20170816	275	2.00	3.93	1.99	8
2193	20170720	275	2.00	3.85	2.09	8
2192	20170623	275	2.00	3.87	2.14	8
2191	20170526	275	2.00	3.63	2.16	8
2190	20170429	275	2.00	3.59	2.20	8
2189	20170402	275	2.00	3.46	2.26	8
2188	20170306	275	2.00	3.60	2.33	8
2187	20170206	275	2.00	3.66	2.32	8
2186	20170110	275	2.00	3.79	2.33	8
2185	20161214	250	2.00	4.05	2.27	9
2184	20161116	250	2.00	4.18	2.22	9
2183	20161020	250	2.00	4.25	2.11	9
2182	20160923	250	2.00	4.17	2.18	9
2181	20160826	250	2.00	4.15	2.17	9
2180	20160730	250	2.00	4.10	2.18	9
2179	20160703	250	2.00	4.22	2.15	9
2178	20160606	250	2.00	4.37	2.19	13
2177	20160510	250	2.00	4.57	2.37	13
2176	20160412	250	2.00	4.70	2.51	13
2175	20160316	250	2.00	4.81	2.56	13
2174	20160218	275	2.00	4.97	2.62	13
2173	20160121	275	2.00	4.87	2.55	13
2172	20151225	275	2.00	4.70	2.50	13
2171	20151128	300	3.00	4.62	2.39	8
2170	20151031	300	3.00	4.77	2.30	8
2169	20151004	275	3.00	4.77	2.18	8
2168	20150907	275	3.00	4.66	2.09	8
2167	20150811	275	3.00	4.29	2.02	8
2166	20150714	250	3.00	4.43	2.10	8
2165	20150617	250	3.00	4.54	2.32	7

Table 2
(Continued)

CR	Start Time	V_s (km s^{-1})	a_2 (deg)	B_0 (nT)	N_0 (cm^{-3})	$L_{\max}$
2164	20150521	250	4.00	4.84	2.64	6
2163	20150424	275	4.00	4.88	2.71	6
2162	20150327	275	4.00	5.03	2.61	6
2161	20150228	275	4.00	5.15	2.42	6
2160	20150201	275	4.00	5.32	2.38	6
2159	20150104	275	4.00	5.21	2.25	6
2158	20141208	300	3.00	4.95	2.22	7
2157	20141111	300	3.00	4.82	2.14	8
2156	20141014	300	3.00	4.58	2.01	9
2155	20140917	300	3.00	4.24	1.78	10
2154	20140821	300	3.00	3.89	1.73	11
2153	20140725	250	2.00	3.74	1.70	11
2152	20140628	250	2.00	3.89	1.72	11
2151	20140531	250	2.00	3.88	1.63	11
2150	20140504	275	2.00	3.98	1.67	11
2149	20140407	275	2.00	3.96	1.57	11
2148	20140311	275	2.00	3.87	1.50	11
2147	20140211	275	2.00	3.71	1.38	12
2146	20140115	275	2.00	3.60	1.36	13
2145	20131219	250	2.00	3.54	1.39	14
2144	20131121	250	2.00	3.33	1.38	14
2143	20131025	250	2.00	3.37	1.48	14
2142	20130928	250	2.00	3.61	1.52	14
2141	20130831	275	2.00	3.96	1.61	14
2140	20130804	275	2.00	4.13	1.74	14
2139	20130708	275	2.00	3.98	1.78	14
2138	20130611	250	2.00	3.81	1.77	14
2137	20130515	250	2.00	3.66	1.78	14
2136	20130417	250	2.00	3.67	1.87	14
2135	20130321	250	2.00	3.61	1.93	14
2134	20130222	250	2.00	3.52	1.77	14
2133	20130125	250	2.00	3.62	1.64	14
2132	20121229	250	2.00	3.78	1.53	11
2131	20121202	250	2.00	3.93	1.52	11
2130	20121104	250	2.00	3.90	1.54	11
2129	20121008	250	2.00	3.91	1.57	11
2128	20120911	275	2.00	4.21	1.63	11
2127	20120815	275	2.00	4.38	1.63	11
2126	20120718	275	2.00	4.36	1.63	11
2125	20120621	275	2.00	4.11	1.65	11
2124	20120525	275	2.00	4.07	1.81	11
2123	20120428	275	2.00	4.16	1.98	11
2122	20120331	275	2.00	4.13	2.03	11
2121	20120304	275	2.00	3.86	1.94	11
2120	20120206	275	2.00	3.67	1.74	11
2119	20120109	275	2.00	3.69	1.58	11
2118	20111213	250	2.00	3.87	1.63	9
2117	20111116	250	2.00	3.89	1.68	9
2116	20111019	250	2.00	3.72	1.69	9
2115	20110922	275	2.00	3.66	1.59	9
2114	20110826	275	2.00	3.78	1.64	9
2113	20110730	275	2.00	3.91	1.83	9
2112	20110703	275	2.00	3.77	1.79	9
2111	20110605	275	2.00	3.87	1.71	9
2110	20110509	275	2.00	3.89	1.59	9
2109	20110412	275	2.00	3.81	1.67	9
2108	20110316	275	2.00	3.47	1.72	9
2107	20110216	275	2.00	3.14	1.76	9
2106	20110120	275	2.00	3.24	1.76	9
2105	20101224	250	2.00	3.26	1.78	10
2104	20101126	250	2.00	3.32	1.65	10
2103	20101030	250	2.00	3.13	1.58	10
2102	20101003	250	2.00	3.11	1.53	10
2101	20100905	250	2.00	3.04	1.55	10

Table 2
(Continued)

CR	Start Time	V_s (km s^{-1})	a_2 (deg)	B_0 (nT)	N_0 (cm^{-3})	$L_{\max}$
2100	20100809	250	2.00	3.29	1.64	10
2099	20100713	250	2.00	3.28	1.67	10
2098	20100616	250	2.00	3.55	1.75	10
2097	20100519	250	2.00	3.45	1.65	10
2096	20100422	250	2.00	3.71	1.51	10
2095	20100326	250	2.00	3.48	1.44	10
2094	20100227	250	2.00	3.34	1.44	10
2093	20100130	250	2.00	2.86	1.50	10
2092	20100103	250	2.00	2.80	1.52	10
2091	20091207	250	2.00	2.73	1.51	15
2090	20091109	250	2.00	2.76	1.51	15
2089	20091013	250	2.00	2.74	1.48	15
2088	20090916	250	4.00	2.84	1.45	15
2087	20090820	250	4.00	2.83	1.52	15
2086	20090723	250	4.00	2.73	1.48	15
2085	20090626	250	2.00	2.62	1.49	15
2084	20090530	250	2.00	2.66	1.45	15
2083	20090503	250	2.00	2.71	1.55	15
2082	20090405	250	2.00	2.82	1.61	15
2081	20090309	250	2.00	2.87	1.61	15
2080	20090210	250	2.00	2.95	1.60	15
2079	20090113	250	3.00	2.90	1.59	15
2078	20081217	250	3.00	2.90	1.57	11
2077	20081120	250	3.00	2.90	1.59	11
2076	20081023	250	3.00	2.88	1.61	11
2075	20080926	250	3.00	2.86	1.63	11
2074	20080830	250	3.00	2.79	1.63	11
2073	20080803	250	3.00	2.90	1.63	11
2072	20080706	250	3.00	2.93	1.69	11
2071	20080609	250	3.00	3.06	1.67	8
2070	20080513	250	3.00	3.08	1.69	8
2069	20080416	250	3.00	3.16	1.69	8
2068	20080320	250	3.00	3.13	1.74	8
2067	20080221	250	3.00	3.09	1.78	8
2066	20080125	250	3.00	3.09	1.86	8
2065	20071229	250	2.00	3.03	1.87	6
2064	20071201	250	2.00	2.99	1.82	6
2063	20071104	250	2.00	2.92	1.74	6
2062	20071008	250	2.00	2.90	1.75	6
2061	20070910	250	2.00	2.97	1.78	6
2060	20070814	250	2.00	3.07	1.77	6
2059	20070718	250	2.00	3.23	1.82	6
2058	20070621	250	2.00	3.23	1.87	6
2057	20070524	250	2.00	3.24	1.95	6
2056	20070427	250	2.00	3.27	1.86	6
2055	20070331	250	2.00	3.41	1.83	6
2054	20070304	250	2.00	3.41	1.90	6
2053	20070204	250	2.00	3.69	1.93	6
2052	20070108	250	2.00	3.60	2.02	6
2051	20061212	250	2.00	3.54	2.03	6

field is modeled to be constant, and it reverses sign at the heliosphere current sheet, which is embedded in low-speed streams between latitudes of $-30°$ and $30°$. At high latitudes of above $50°$, the velocity is nearly uniformly of high speed. Streams of different speeds alternate at low latitudes. When the boundary and initial conditions are given, it takes $\sim$200 hr to reach the MHD equilibrium state.

Figure 2 shows the distribution of the radial velocity V_r, number density N, temperature T, and magnetic field strength B

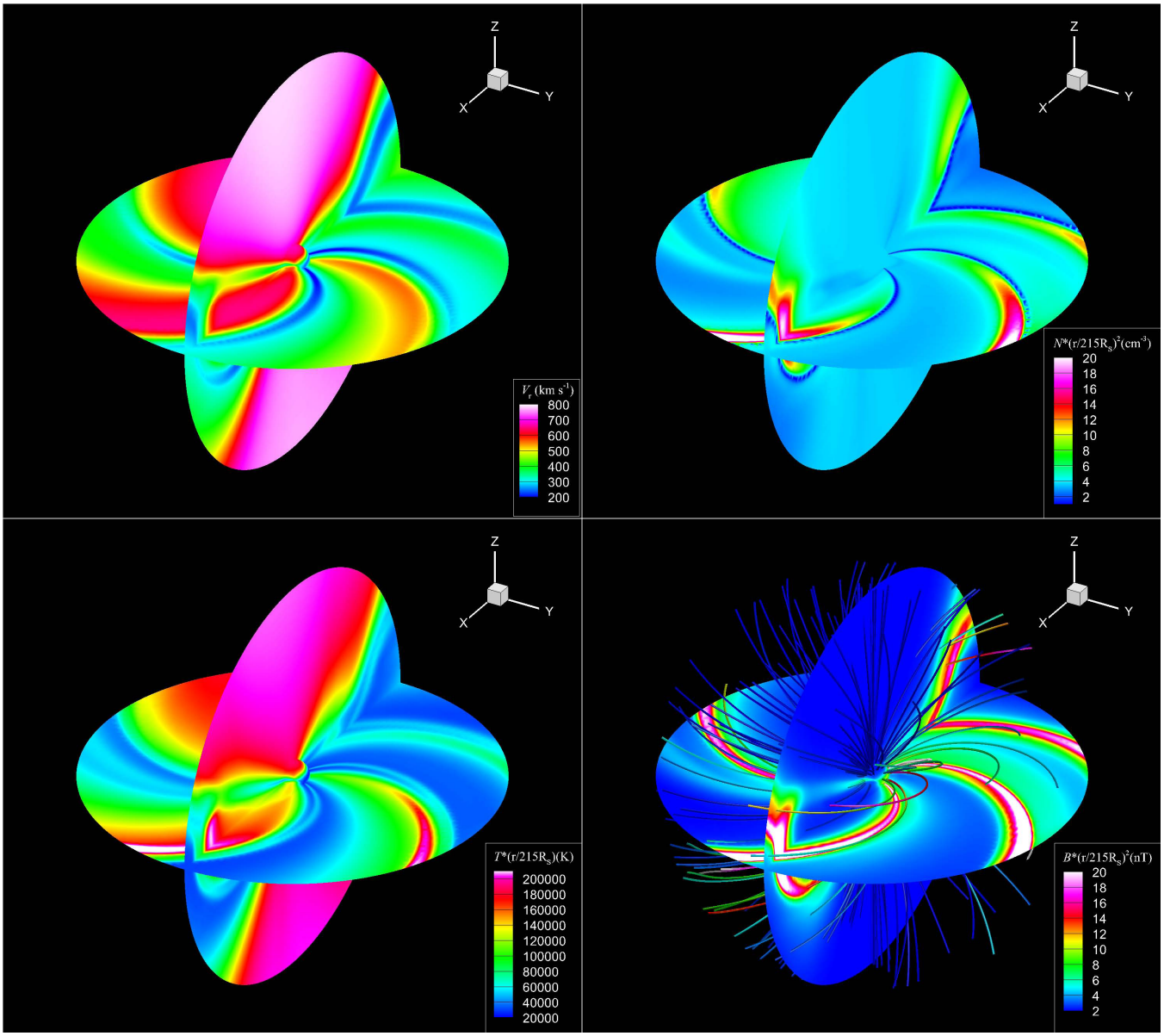

Figure 2. Maps of simulated solar wind parameters in the heliospheric equatorial plane and meridional plane for CR2053. From the upper left to the lower right, the panels show velocity V_r (km s^{-1}), number density N (cm^{-3}), temperature T (K), and magnetic field strength B_r (nT) and magnetic field lines.

(with the magnetic field lines) in the heliospheric equatorial plane and the meridional plane of steady state. To better illustrate the features in the figures, we normalize N, T, and B to 1 au by using the factors of r^2, r, and r^2, respectively. From Figure 2, the classic features of interplanetary solutions—that is, the high-density corotating interaction regions between fast and slow solar wind streams—can be clearly recognized. Near the north pole and south pole in the heliospheric meridional plane, high-speed wind is seen to dominate. However, there is a mix of slow and fast winds at all latitudes, arising from the coronal structure present at this time period.

Figure 3 shows the distribution of the simulated parameters at 1 au for CR2053 when the lower-boundary condition is determined by that displayed in Figure 1. In contrast with that at the lower boundary, the physical parameters at 1 au have changed in their distribution with varying degrees. For the distribution of all parameters, there is a left shift of about 50° in longitudinal direction, which is a reflection of the rotation effect of the Sun. In low latitudes, a few compression and rarefaction regions are formed due to the interaction of the high-speed streams (HSSs) and the low-speed streams (Gosling et al. 1972; Gosling & Pizzo 1999). The density and magnetic field in the compression regions are much higher than that in other locations. The temperatures in the intervals of increasing speed are slightly higher than that of decreasing speeds, indicating that the adiabatic compression increases the temperature.

To verify and validate our model, we make a comparison with the in situ measurement near the Earth. We obtained the observational data from the OMNI website (http://omniweb.gsfc.nasa.gov), which includes the hourly averaged in situ data from *Wind* (Gloeckler et al. 1995) and the *Advanced Composition Explorer* (*ACE*; Stone et al. 1998). Considering the radial and latitudinal changes of the spacecraft's orbit during the course of one CR, we obtain the simulation values at the L1 point per hour through interpolation and then make a comparison with the hourly averaged observational data.

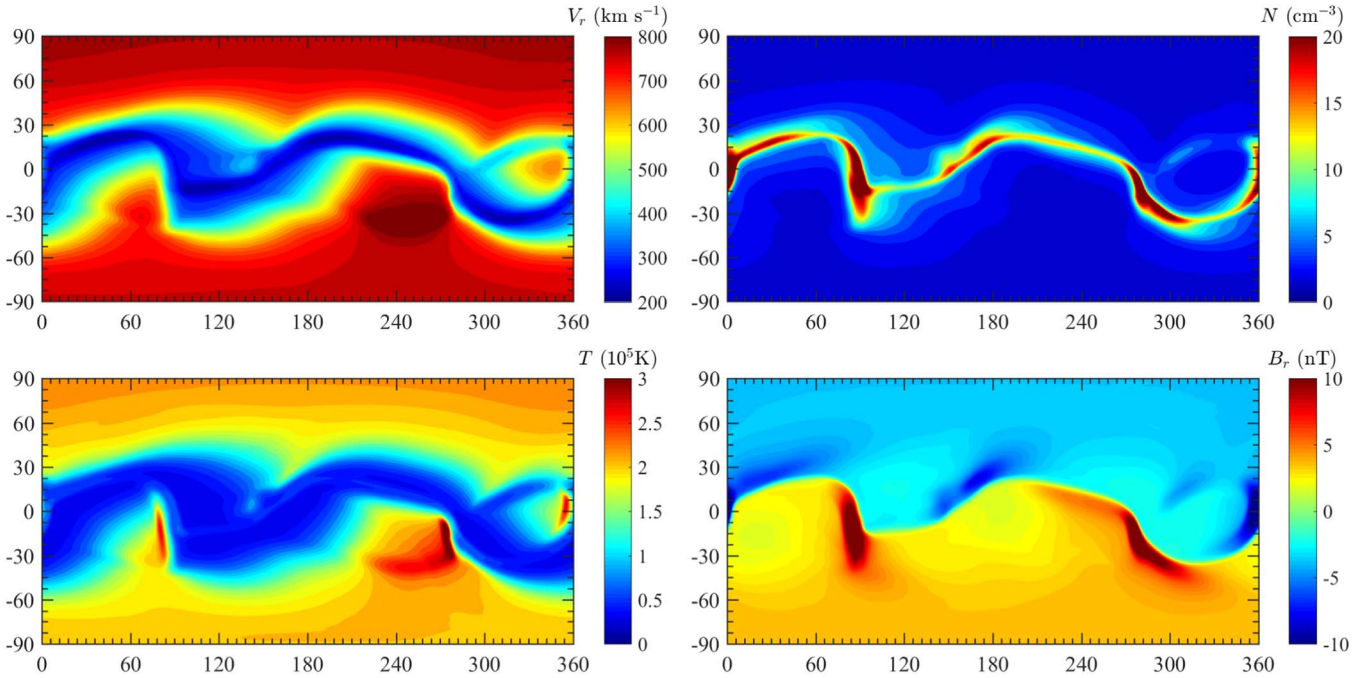

Figure 3. Maps of simulated solar wind parameters at 1.0 au for CR2053. From the upper left to the lower right, the panels show the velocity V_r (km s^{-1}), number density N (cm^{-3}), temperature T (K), and radial magnetic B_r (nT). For each panel, the x axis is longitude, and the y axis is latitude.

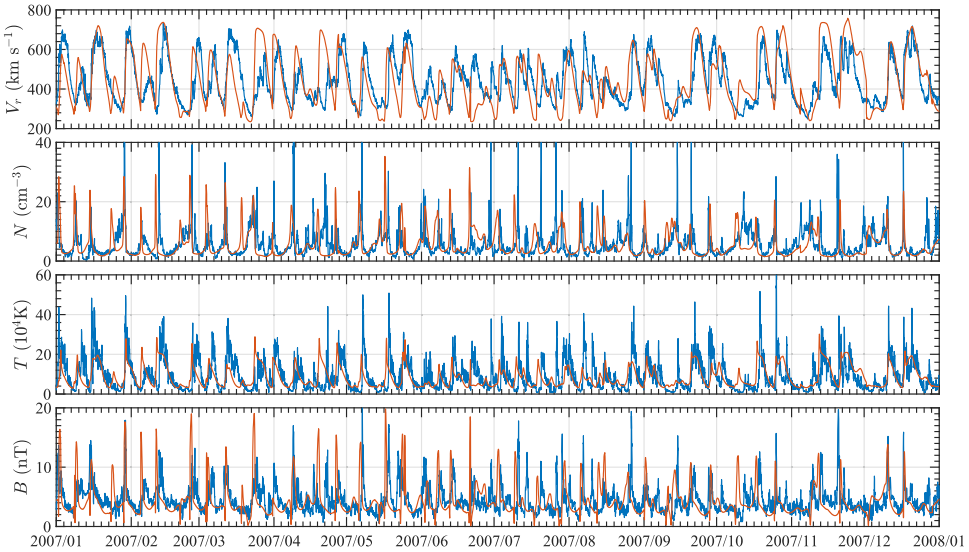

Figure 4. Modeled (red lines) and observed (blue lines) time profiles of solar wind parameters at 1.0 au through all of 2007. The data points are sampled every hour. From the top to the bottom, the panels show the speed V_r (km s^{-1}), number density N (cm^{-3}), temperature T (K), and total magnetic field strength B (nT).

The comparison of the modeled results with the in situ data throughout 2007 is shown in Figure 4. From the top to the bottom are the solar wind speed V_r, number density N, temperature T, and total magnetic field strength B. The blue lines represent the observation, and the red lines are simulated results. During 2007, the simulation could catch most of the HSSs. Moreover, the duration time and the magnitude of the HSSs are largely consistent with that of the observations.

To give a detailed comparison on HSSs, we compare the observed and modeled HSSs at 1 au during 2007. The existence of HSSs and the positions of the stream interfaces are indicated by the black vertical lines in Figure 5. Here we define the HSSs as the region where the solar wind speed increases from 400 km s^{-1} to at least 550 km s^{-1} within 24 hr. From the observations, there are 34 such HSSs in 2007, and from the simulation, there are 34 HSSs, among which 29 are consistent with the observations. Therefore, our model successfully reproduces about 85% of observed HSSs and misses 15% of HSSs, and the "false-alarm rate" is also 15%. The HSS arrival time error Δt can be defined as the time discrepancy between the observed and modeled stream interfaces, shown as the black vertical lines in Figure 5, which is

$$\Delta t = t^m - t^o, \text{ and } \quad |\Delta t| = |t^m - t^o|. \tag{16}$$

For all 29 observed HSSs hit by the simulation, the average Δt is 4 hr, and the standard error of Δt is 21 hr; the average $|\Delta t|$ is 17 hr, and the standard error is 13 hr.

To give a detailed comparison of magnetic field, B_r is shown in the bottom panels of Figures 6, indicating the in-ecliptic IMF

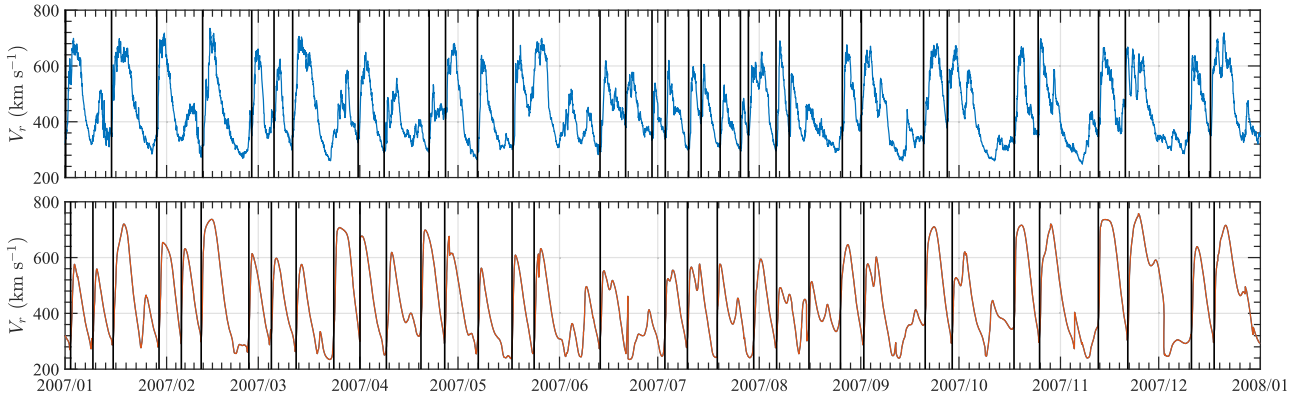

Figure 5. Observed (top panel) and modeled (bottom panel) HSSs near the Earth during 2007. The stream interfaces are marked by the black vertical lines.

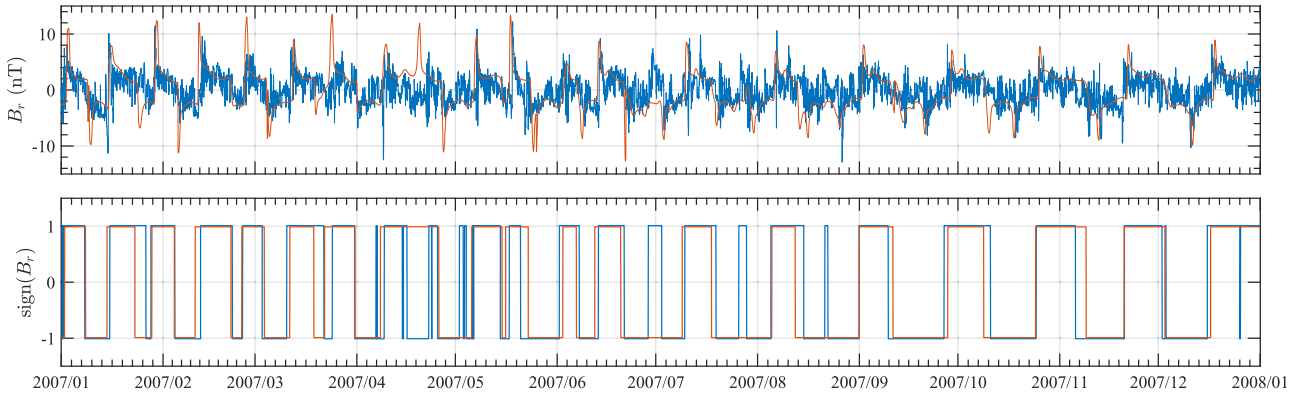

Figure 6. Modeled (red lines) and observed (blue lines) radial magnetic field B_r (nT; top panel) and the sign of B_r (bottom panel) at 1 au during 2007.

polarity at Earth. The positive B_r means the polarity is outward from the Sun; otherwise, it is inward toward the Sun. From the B_r panel in Figure 6, we see that our simulation can reproduce most of the pattern of B_r and the in-ecliptic IMF polarity at Earth. Moreover, by smoothing the data from both observation and simulation using a 72-point moving average, we can deduce that our model successfully catches 85% of observed in-ecliptic IMF polarity. The average time discrepancy Δt between observed and modeled polarity reversals is -5 hr, and the standard error of Δt is 33 hr; the average $|\Delta t|$ is 24 hr, and the standard error is 22 hr. The negative sign of Δt indicates that our model tends to predict an earlier arrival of polarity reversal.

Based on the visual inspection of the plots in Figures 4–6, the simulation reproduces most of the patterns of the large-scale structures: HSS, corotating interaction region (CIR) and sector boundary. From Figure 4, we notice that if the speed is well simulated, the density and magnetic field can also fit the observations well, especially during the time intervals when the arrival times of HSSs coincide with that of the observations. Therefore, for the ambient solar wind without transient events, an accurate speed boundary condition is very important for predicting the magnetic field strength.

To quantitatively assess our model performance in the prediction of ambient solar wind conditions in near-Earth space, we also present a few statistical analysis results from the model and observations in 2007. If the observed (modeled) value of a parameter at time t is denoted by $x_t^o(x_t^m)$, then the mean value of the observation $\overline{x_t^o}$ ($\overline{x_t^m}$), the root-mean-square error (RMSE) of N observations, and the correlation coefficient (cc) can be given by

$$\overline{x_t^o} = \frac{1}{N}\sum_{t=1}^{N} x_t^o, \tag{17}$$

$$\overline{x_t^m} = \frac{1}{N}\sum_{t=1}^{N} x_t^m, \tag{18}$$

$$\mathrm{RMSE} = \sqrt{\frac{1}{N}\sum_{t=1}^{N}(x_t^o - x_t^m)^2}, \tag{19}$$

and

$$\mathrm{cc} = \frac{\sum_{t=1}^{N}(x_t^o - \overline{x_t^o})^2(x_t^m - \overline{x_t^m})^2}{\sum_{t=1}^{N}(x_t^o - \overline{x_t^o})^2\sum_{t=1}^{N}(x_t^m - \overline{x_t^m})^2}. \tag{20}$$

Table 3
Comparative Analysis of Measured Values and Simulated Values for 2007

Parameters (Unit)	$\overline{x_t^o}$	$\overline{x_t^m}$	RMSE	cc
V_r (km s^{-1})	441	444	109	0.63
N (cm^{-3})	5.7	5.4	5.8	0.28
T (10^4 K)	9.1	8.4	6.8	0.51
B (nT)	4.5	4.2	3.0	0.27
B_r (nT)	−0.01	−0.05	3.3	0.45

Table 3 lists the mean value of observation x_t^o, mean value of model x_t^m, RMSE, and cc of our model in 2007. It can be found that all of the mean values of the four simulated parameters are

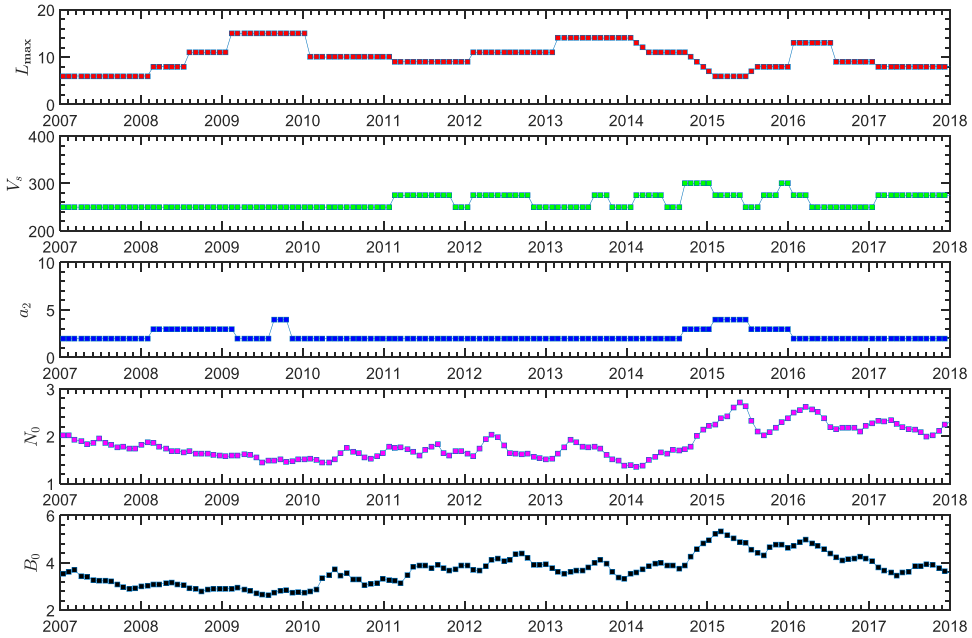

Figure 7. Value of the free parameters in the boundary conditions from 2007 to 2017. From the top to the bottom, the parameters are L_{max}, V_s (km s^{-1}), a_2 (deg), N_0 (cm^{-3}), and B_0 (nT).

very similar to that of the observational data. The RMSE of the solar wind speed is 109 km s^{-1}, and the cc reaches 0.64, which is the highest among all parameters. Although the simulated number density seems to closely follow the general pattern of observation in the visual comparison, e.g., the simulated profile could reproduce most of the HSSs and low-speed streams in 2007, as shown in Figure 4, its RMSE is 5.8 cm^{-3}, which is as much as the mean value of the observation, and the cc is only 0.28. If adopting $\rho \propto V^{-2}$ at the lower boundary and tuning the momentum flux to make the simulation results at the L1 point consistent with the observations, we would get a density value at the high-latitude region about 20% lower than the *Ulysses* observation. If adopting $\rho \propto V^{-1}$ at the lower boundary and tuning the mass flux to make the simulation results at the L1 point consistent with the observations, we would get a density value at the high-latitude region about 75% larger than the *Ulysses* observation. In our opinion, Equation (8) can reflect the relationship between the number density and solar wind speed at 0.1 au more accurately. Although the RMSE of the temperature is ∼69% of the mean observation value, the cc is over 0.5. The mean value of the magnetic field from the simulation is only ∼6% smaller than that from the observation at 1 au, which indicates that the distribution of the magnetic field chosen at the lower boundary is quite reasonable.

Gressl et al. (2014) also simulated the background solar wind in 2007 by using different models with synoptic maps from MDI, NSO, MWO, and GONG separately, which were the MAS/MAS (MDI), MAS/ENLIL (NSO), WSA/ENLIL (NSO), WSA/ENLIL (MWO), and WSA/ENLIL (GONG) models. Their results showed that both the MAS/MAS and MAS/ENLIL models obviously overestimated the density in the low-speed streams; e.g., MAS/ENLIL tended to overestimate the density peaks by up to a factor of 2, while for all the ENLIL models, the simulated temperature was systematically underestimated by about an order of magnitude. And, for all of the models, the simulated total magnetic field strength is as small as at least a factor of 2, compared with the observation. We compare the ccs deduced from our improved IN-TVD model and the hybrid WSA/ENLIL model with the same temporal resolution of 1.8 hr and the same synoptic maps input from GONG presented in Gressl et al. (2014) during 2007, as shown in Table 4. It can be found that the ccs from our model are about 0.02–0.18 higher than the WSA/ENLIL model. Moreover, for the parameters of solar wind speed, number density, temperature, total magnetic field strength and radial magnetic field at 1 au deduced from our improved 3D IN-TVD model, there are no obvious systematic overestimation or underestimation, as shown in Figure 4.

Table 4
Comparative Analysis of ccs between Our Results and the Results Deduced from the WSA/ENLIL Model for 2007

Models	V_r (km s^{-1})	N (cm^{-3})	T (10^4 K)	B (nT)	B_r (nT)
Improved IN-TVD (GONG)	0.63	0.28	0.51	0.27	0.45
WSA/ENLIL (GONG)*	0.53	0.16	0.33	0.18	0.43

4.2. Results from 2008 to 2017

To further test the performance of our model, we simulate the background solar wind from 2008 to 2017, which covers the period from the solar minimum of the 23rd solar cycle to the decay phase of the 24th solar cycle. As we mentioned in Section 3, there are five free parameters in the boundary condition, among which B_0 and N_0 are restricted from the historical observational data at 1 au. Here L_{max} is the primary regulatory factor, and V_s and a_2 are the secondary regulatory parameters. In general, the procedure of tuning L_{max}, V_s, and a_2 can be summarized as follows. (1) First, the base values of L_{max}, V_s, and a_2 are set as 9 and 250 km s^{-1} and 2°, respectively. (2) Second, these three parameters can be adjusted according to the simulation results with the base values. For example, if the simulated velocity in HSSs is generally higher or the time span of HSSs is larger than the observations, L_{max} and a_2 should be increased properly. (3) Finally, based on items (1) and (2), V_s could be tuned slightly. Figure 7 gives the

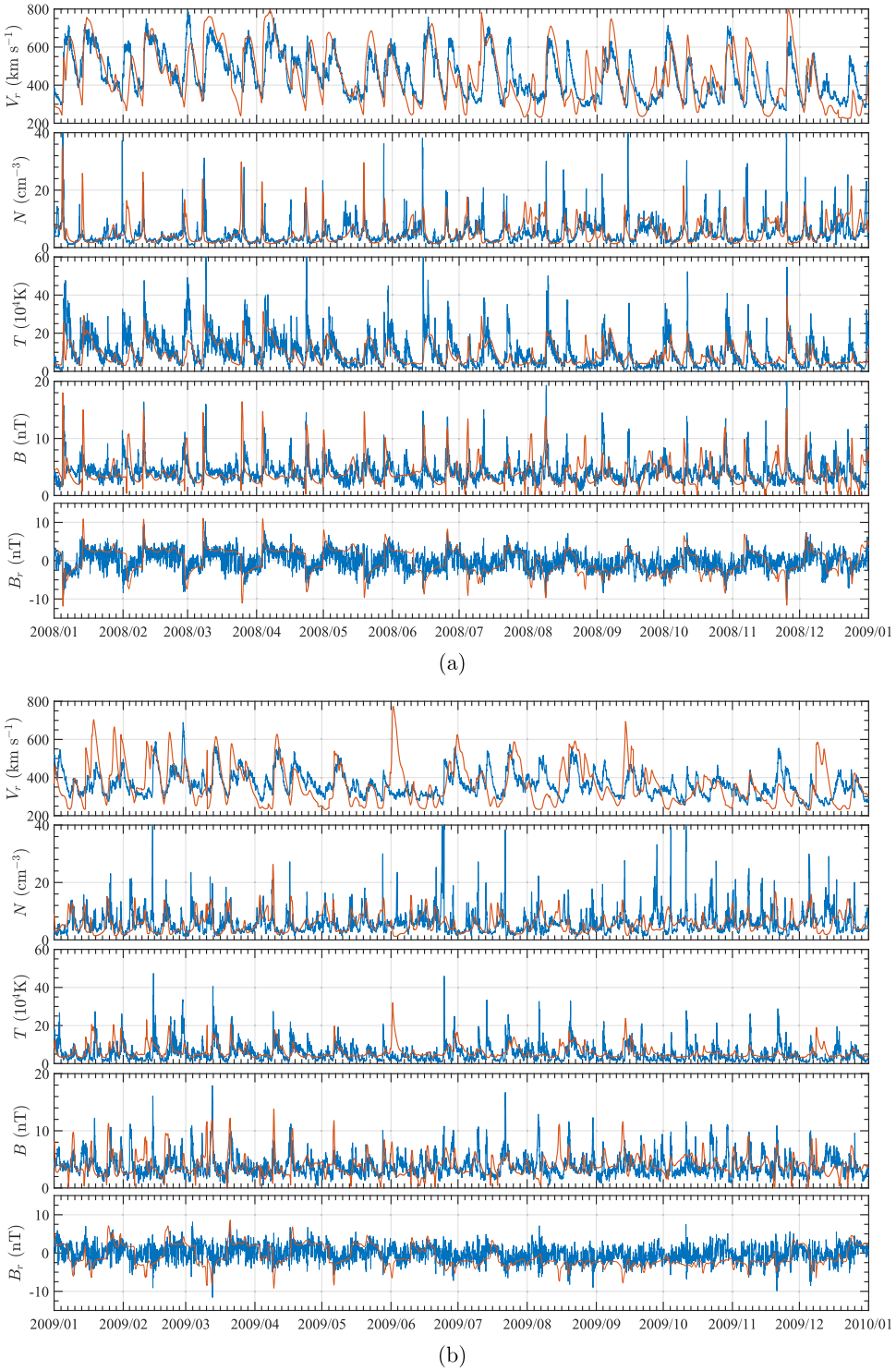

Figure 8. Modeled (red lines) and observed (blue lines) profiles of solar wind parameters at 1 au from 2008 (panel (a)) to 2017 (panel (j)). For each year, solar wind speed V_r (km s^{-1}), number density N (cm^{-3}), temperature T (K), total magnetic field strength B (nT), and radial magnetic field strength B_r (nT) are shown. (An extended version of this figure is available.)

variation of the free parameters used in the lower-boundary conditions from 2007 to 2017, in which one point represents one CR. It can be found that these parameters can be kept unchanged for quite a long period (from a few CRs to several years). Table 2 provides the values of the free parameters in the lower-boundary conditions from 2007 to 2017. In real-time prediction, we can update the $L_{\max}$, V_s, and a_2 according to the observed solar wind speed at 1 au in the most recent CR using the procedures mentioned above.

Figure 8 presents the comparison of the modeled and observed solar wind parameters at 1 au from 2008 to 2017. Moreover, to show the comparison more clearly, we also enlarge the comparison between the modeled results and the observations in four CRs located at different phases of solar

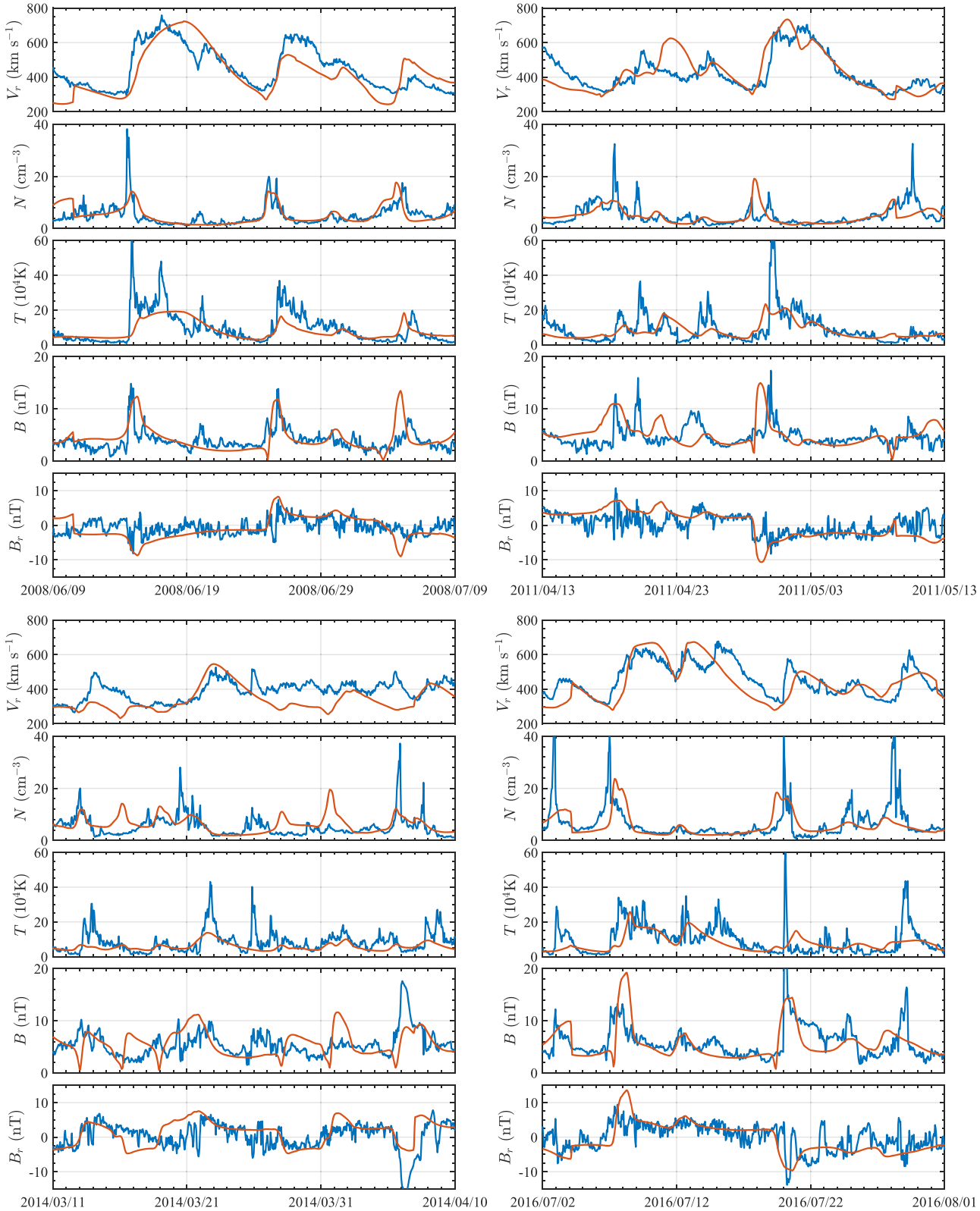

Figure 9. Modeled (red lines) and observed (blue lines) profiles of solar wind parameters at 1 au located at different phases of solar activity: CR2071 in 2008, CR2109 in 2010, CR2148 in 2014, and CR2179 in 2016. For each CR, solar wind speed V_r(km s^{-1}), number density N (cm^{-3}), temperature T (K), total magnetic field strength B (nT), and radial magnetic field strength B_r (nT) are shown.

activity: CR2071 in 2008, CR2109 in 2010, CR2148 in 2014, and CR2179 in 2016, as shown in Figure 9. Correspondingly, Table 5 gives the comparative analysis of measured and simulated values from 2008 to 2017, similar to Table 3. All panels of Figures 8 and 9 show the simulation results, as well as the in situ measurements from the OMNI observations for all parameters under study: solar wind speed V_r, proton density N, temperature T, total magnetic field strength B, and radial magnetic

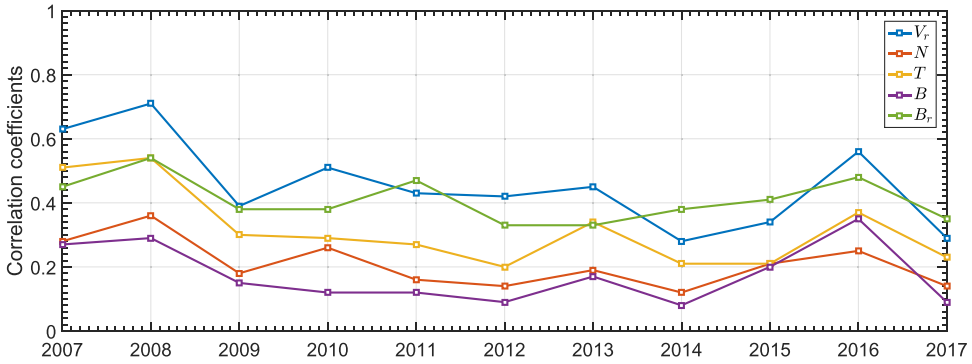

Figure 10. Distribution of ccs between modeled and observed solar wind parameters (V_r, N, T, B, and B_r) in difference phases of solar cycle 24.

Table 5
Values of the Free Parameters in Boundary Conditions from 2007 to 2017

Year	Parameters (Unit)	$\overline{x_t^o}$	$\overline{x_t^m}$	RMSE	cc
2008	V_r (km s^{-1})	451	449	103	0.71
	N (cm^{-3})	5.0	4.9	4.3	0.36
	T (10^4 K)	9.7	8.7	6.9	0.54
	B (nT)	4.2	3.9	2.4	0.29
	B_r (nT)	−0.12	−0.14	2.8	0.54
2009	V_r (km s^{-1})	365	363	100	0.40
	N (cm^{-3})	6.0	5.7	4.8	0.18
	T (10^4 K)	5.3	6.0	4.7	0.30
	B (nT)	3.9	3.9	2.3	0.15
	B_r (nT)	−0.17	−1.0	2.8	0.38
2010	V_r (km s^{-1})	403	368	103	0.52
	N (cm^{-3})	5.6	5.6	4.8	0.26
	T (10^4 K)	7.5	6.1	6.5	0.29
	B (nT)	4.7	4.6	2.8	0.12
	B_r (nT)	−0.32	−0.28	3.3	0.38
2011	V_r (km s^{-1})	421	405	103	0.43
	N (cm^{-3})	5.4	5.2	5.3	0.16
	T (10^4 K)	9.0	7.0	8.7	0.27
	B (nT)	5.3	5.1	3.2	0.12
	B_r (nT)	−0.46	−0.47	3.1	0.47
2012	V_r (km s^{-1})	408	365	103	0.42
	N (cm^{-3})	5.6	5.8	4.9	0.14
	T (10^4 K)	7.9	6.0	8.4	0.20
	B (nT)	5.7	5.4	3.8	0.09
	B_r (nT)	−0.37	−0.13	4.0	0.33
2012	V_r (km s^{-1})	408	365	103	0.42
	N (cm^{-3})	5.6	5.8	4.9	0.14
	T (10^4 K)	7.9	6.0	8.4	0.20
	B (nT)	5.7	5.4	3.8	0.09
	B_r (nT)	−0.37	−0.13	4.0	0.33
2013	V_r (km s^{-1})	397	343	99	0.45
	N (cm^{-3})	5.7	5.9	5.1	0.19
	T (10^4 K)	7.3	5.2	7.7	0.34
	B (nT)	5.2	5.3	3.0	0.17
	B_r (nT)	0.08	0.51	3.8	0.33
2014	V_r (km s^{-1})	398	373	110	0.28
	N (cm^{-3})	6.2	5.9	5.2	0.12
	T (10^4 K)	8.1	6.4	8.0	0.21
	B (nT)	6.0	5.5	3.6	0.08
	B_r (nT)	0.01	0.91	4.2	0.38
2015	V_r (km s^{-1})	437	422	119	0.34
	N (cm^{-3})	7.2	7.2	7.3	0.21
	T (10^4 K)	9.7	7.8	9.3	0.21
	B (nT)	6.7	6.3	4.1	0.20
	B_r (nT)	0.75	1.08	4.7	0.41
2016	V_r (km s^{-1})	446	434	109	0.56
	N (cm^{-3})	6.8	6.7	6.5	0.25
	T (10^4 K)	10.2	8.1	8.4	0.37
	B (nT)	6.1	5.9	3.4	0.35
	B_r (nT)	0.22	0.42	4.2	0.48
2017	V_r (km s^{-1})	455	432	131	0.29
	N (cm^{-3})	6.5	6.2	6.2	0.14
	T (10^4 K)	10.2	7.9	10.2	0.23
	B (nT)	5.2	4.9	3.4	0.09
	B_r (nT)	0.25	0.79	4.1	0.35

field B_r. We also plot the cc of the five parameters versus year in Figure 9. The best results are obtained in 2008, and the ccs of V_r, N, T, B, and B_r are 0.71, 0.36, 0.54, 0.29, and 0.54, which are a little higher that the simulation results in 2007. We also find that all of the mean values of the four simulated parameters are very similar to those of the observational data. For the number density, the cc is 0.36, while the simulated density profiles could reproduce most of the HSSs and low-speed streams in 2008. The mean value of the magnetic field strength from the simulation is only ∼7% smaller than that from the observation at 1 au. The best fit in 2008 is probably due to a near-solar minimum; i.e., very few CME events occurred, and there were steady HSSs in this year. The lowest agreement between the models and observations was found in 2014, and the ccs of V_r, N, T, B, and B_r are only 0.28, 0.12, 0.21, 0.08, and 0.38. This year is near the solar maximum; thus, the solar activity was much higher than in other years, and CME events occurred more frequently. From Table 5 and Figure 10, we also find that the main trend of all the ccs first decreases from 2007 to 2014 and then increases from 2014 to 2016, which is roughly consistent with the solar activity.

As seen from Figure 10 and Table 5, the best result of the parameters is solar wind speed, and the ccs are above 0.28 for all 11 yr from 2007 to 2017 and above 0.4 for 8 yr. The ccs of temperature, number density, and radial magnetic field change from 0.20 to 0.54, from 0.12 to 0.36, and from 0.33 to 0.54. The lowest agreement between the modeled results and observations was found for the total magnetic field strength with ccs between 0.08 and 0.35, as shown in Figure 10.

Moreover, the average values of the ccs of V_r, N, T, B, and B_r are 0.46, 0.21, 0.32, 0.18, and 0.41, respectively.

From the comparison of the annual average values between observation and simulation ($\overline{x_t^o}$ and $\overline{x_t^m}$) in Table 5, it can be found that for all parameters V_r, N, T, B, and B_r from 2007 to 2017, there is no obvious systematic overestimation or underestimation. Especially for the total magnetic field strength B, in the models mentioned by Gressl et al. (2014), the simulated values were always as small as at least a factor of 2; in our simulation, the difference between the annual average value of measured and simulated B is no more than 8.3% for the whole 11 yr.

5. Summary

In this paper, we employ an improved IN-TVD MHD model with a new boundary treatment to simulate the propagation and distribution of the solar wind into the heliosphere. In the improved model, we set the lower boundary at 0.1 au and employ the six-component grid system in the computational domain. The model solves ideal single-fluid MHD equations in the corotating frame by using the TVD Lax–Friedrich scheme.

At the lower boundary, we construct a set of boundary conditions in which we do the following. (1) Based on magnetogram synoptic map images from GONG as input, we use the PFSS model to obtain the polarity of the radial magnetic field and then use the historical observed magnetic field B_0 at 1 au to limit the value of the radial magnetic field. (2) We use the empirical WSA relation to assign the solar wind speed, in which we keep three free parameters. (3) We calculate the density by setting the solar wind energy flux as constant and using the historical observed density N_0 at 1 au. (4) We specify the temperature by using the relationship that the proton temperature is a quadratic function of the velocity at 1 au and normalizing T_p to 21.5 R_s by the power law $T_p \sim 1/r^{2(\gamma-1)}$. In the boundary conditions, we only reserve five free parameters that slowly vary with time, so as to simulate the solar wind for different phases of the solar cycle and to improve the prediction of the solar wind parameters, while all other free parameters are kept constant across the solar cycle. Two of the five adjustable parameters, B_0 and N_0, are calculated based on the historical observational data of the past three CRs at 1 au and do not need to be tuned. For the remaining three free parameters, V_s and a_2 are the parameters in the WSA solar wind model and only need to be tuned slightly. Here $L_{\max}$, which is the number of multipole components included in the spherical harmonic expansion in the PFSS model, has the most prominent effect on the model results, but it is very simple to tune this parameter. Our model can run stably and efficiently for a long time and is suitable for different phases of the solar cycle.

Using the improved IN-TVD model with the new lower-boundary conditions, we simulated the background solar wind from 2007 to 2017. By tuning very few parameters, our simulation could reproduce most of the characteristic solar wind structures, e.g., HSSs and sector boundaries, as well as the amplitudes of the solar wind parameters near the Earth, including the solar wind speed, number density, temperature, and magnetic field. The consistency in observations of all parameters suggests that our modeling approach is suitable for predicting ambient solar wind in the heliosphere.

In our model, there are only three parameters for tuning freely; further, based on the simulation of the past 11 yr, these parameters can remain unchanged for quite a long time (several CRs to several years). Therefore, the improved IN-TVD model with the new boundary treatment can be applied for the prediction/forecast of the solar wind parameters near the Earth. Among the 11 yr of calculation, the best results were obtained in 2007 and 2008, and the lowest agreement between the modeled results and observations was found in 2014. This shows that transient solar activity can complicate the performance of the model of the ambient solar wind. The trend is roughly consistent with solar activity, which indicates that near the solar maximum, considering the influence of transient CME events on the background solar wind modeling is necessary for further improving the prediction.

We acknowledge the use of solar wind data obtained from the GSFC/SPDF OMNI web, synoptic magnetogram from GONG/NSO, and ICME list from the http://www.srl.caltech.edu/ACE/ASC/DATA/level3/icmetable2.htm website by Richardson and Cane. This work is jointly supported by grants from the National Natural Science Foundation of China (41774184, 41474152, 41731067, 41874202, and 41531073) and the Specialized Research Fund for State Key Laboratories. FS is also supported by the National Program for Support of Top-notch Young Professionals.

ORCID iDs

Fang Shen https://orcid.org/0000-0002-4935-6679
Jie Zhang https://orcid.org/0000-0003-0951-2486
Xueshang Feng https://orcid.org/0000-0001-8605-2159

References

Altschuler, M. D., & Newkirk, G. 1969, SoPh, 9, 131
Arge, C. N., Odstrcil, D., Pizzo, V. J., & Mayer, L. R. 2003, in AIP Conf. Ser. 679, Solar Wind Ten, ed. M. Velli et al. (Melville, NY: AIP), 190
Burlaga, L. F., & Ogilvie, K. W. 1970, SoPh, 15, 61
Detman, T., Smith, Z., Dryer, M., et al. 2006, JGRA, 111, A07102
Detman, T. R., Intriligator, D. S., Dryer, M., et al. 2011, JGRA, 116, A03105
Elliott, H. A., McComas, D. J., Schwadron, N. A., et al. 2005, JGRA, 110, A04103
Feng, X., Wu, S. T., Wei, F., & Fan, Q. 2003, SSRv, 107, 43
Feng, X., Xiang, C., Zhong, D., & Fan, Q. 2005, ChSBu, 50, 672
Feng, X., Yang, L., Xiang, C., et al. 2010, ApJ, 723, 300
Feng, X., Zhou, Y., & Wu, S. T. 2007, ApJ, 655, 1110
Feynman, J., & Gabriel, S. B. 2000, JGR, 105, 10543
Gloeckler, G., Balsiger, H., Bürgi, A., et al. 1995, SSRv, 71, 79
Gosling, J. T., Hundhausen, A. J., Pizzo, V., & Asbridge, J. R. 1972, JGR, 77, 5442
Gosling, J. T., & Pizzo, V. J. 1999, SSRv, 89, 21
Gressl, C., Veronig, A. M., Temmer, M., et al. 2014, SoPh, 289, 1783
Hayashi, K. 2012, JGRA, 117, A08105
Hoeksema, J. T., Wilcox, J. M., & Scherrer, P. H. 1983, JGR, 88, 9910
Jian, L. K., MacNeice, P. J., Taktakishvili, A., et al. 2015, SpWea, 13, 316
Le Chat, G., Issautier, K., & Meyer-Vernet, N. 2012, SoPh, 279, 197
Lee, C. O., Luhmann, J. G., Odstrcil, D., et al. 2009, SoPh, 254, 155
Lopez, R. E., & Freeman, J. W. 1986, JGR, 91, 1701
McGregor, S. L., Hughes, W. J., Arge, C. N., Owens, M. J., & Odstrcil, D. 2011, JGRA, 116, A03101
Neugebauer, M., & Snyder, C. W. 1966, JGR, 71, 4469
Odstrcil, D. 2003, AdSpR, 32, 497
Owens, M. J., Spence, H. E., McGregor, S., et al. 2008, SpWea, 6, S08001
Parker, E. N. 1958, ApJ, 128, 664
Phillips, J. L., Bame, S. J., Barnes, A., et al. 1995, GeoRL, 22, 3301
Poduval, B., & Zhao, X. P. 2004, JGRA, 109, A08102
Rempel, M., Schüssler, M., & Knölker, M. 2009, ApJ, 691, 640
Richardson, I. G., & Cane, H. V. 1995, JGR, 100, 23397
Richardson, I. G., & Cane, H. V. 2010, SoPh, 264, 189
Riley, P., Ben-Nun, M., Linker, J. A., Owens, M. J., & Horbury, T. S. 2017, SpWea, 15, 526
Riley, P., Linker, J. A., & Arge, C. N. 2015, SpWea, 13, 154
Schatten, K. H. 1971, CosEl, 2, 232

Schatten, K. H., Wilcox, J. M., & Ness, N. F. 1969, SoPh, 6, 442
Shen, F., Feng, X., & Song, W. B. 2009, Sci. China Ser. E: Technol. Sci., 52, 2895
Shen, F., Feng, X., Wu, S. T., & Xiang, C. 2007, JGR, 112, A06109
Shen, F., Feng, X., & Xiang, C. 2012a, JASTP, 77, 125
Shen, F., Feng, X. S., Wang, Y., et al. 2011a, JGRA, 116, A09103
Shen, F., Feng, X. S., Wu, S. T., Xiang, C. Q., & Song, W. B. 2011b, JGRA, 116, A04102
Shen, F., Shen, C., Wang, Y., Feng, X., & Xiang, C. 2013, GeoRL, 40, 1457
Shen, F., Shen, C., Zhang, J., et al. 2014, JGRA, 119, 7128
Shen, F., Wu, S. T., Feng, X., & Wu, C.-C. 2012b, JGRA, 117, A11101
Shiota, D., Kataoka, R., Miyoshi, Y., et al. 2014, SpWea, 12, 187
Smith, E. J., & Balogh, A. 1995, GeoRL, 22, 3317
Snodgrass, H. B., & Ulrich, R. K. 1990, ApJ, 351, 309
Steinitz, R., & Eyni, M. 1980, ApJ, 241, 417
Stevens, M. L., Linker, J. A., Riley, P., & Hughes, W. J. 2012, JASTP, 83, 22
Stone, E. C., Frandsen, A. M., Mewaldt, R. A., et al. 1998, SSRv, 86, 1
Tóth, G., van der Holst, B., Sokolov, I. V., et al. 2012, JCoPh, 231, 870
Totten, T. L., Freeman, J. W., & Arya, S. 1995, JGR, 100, 13
van der Holst, B., & Keppens, R. 2007, JCoPh, 226, 925
Verbanac, G., Vršnak, B., Živković, S., et al. 2011, A&A, 533, A49
Wang, Y.-M., & Sheeley, N. R., Jr. 1990, ApJ, 355, 726
Wiengarten, T., Kleimann, J., Fichtner, H., et al. 2014, ApJ, 788, 80
Zhao, X. P., & Hoeksema, J. T. 2010, SoPh, 266, 379